Journal of Materials Chemistry A

ROYAL SOCIETY OF CHEMISTRY

COMMUNICATION

View Article Online
View Journal | View Issue

Cite this: J. Mater. Chem. A, 2022, 10, 19612

Received 17th March 2022
Accepted 27th April 2022

DOI: 10.1039/d2ta02092k

rsc.li/materials-a

Sustainable development of graphitic carbon nanosheets from plastic wastes with efficient photothermal energy conversion for enhanced solar evaporation†

Marliyana Aizudin, ‡[a] Ronn Goei, ‡[b] Amanda Jiamin Ong, [b] Yong Zen Tan, [c] Shun Kuang Lua, [c] Rafeeque Poolamuri Pottammel,[d] Hongbo Geng, [e] Xing-Long Wu, [f] Alfred Ling Yoong Tok *[b] and Edison Huixiang Ang *[a]

We demonstrate that by a simple solvothermal treatment followed by carbonization, plastic waste can be turned into graphitic carbon nanosheets, with an excellent photothermal conversion efficiency (99%) that is capable of generating a high evaporation rate (1.50 L m^{-2} h^{-1} at 1 kW m^{-2}) in a solar evaporator, and these are among the best values reported thus far.

Global plastic pollution is expected to be 8.3 billion metric tonnes from 1950 to the present, and with the outbreak of the COVID-19 pandemic, there has been a significant surge in household plastic waste, resulting in a global waste management crisis.[1,2] Improper plastic waste management can have a negative impact on the environment, wildlife, and public health.[3,4] To address this concern, traditional recycling plastic strategies, such as mechanical methods, have been used to convert plastic waste into feedstock, however, the resulting products generally have limited structural designs and inferior properties, limiting their range of application.[5,6] For this reason, advanced plastic waste recycling technologies are becoming increasingly important for discovering new recycled materials with beneficial properties that can improve industrial processes while also helping the nation to meet global sustainability goals.[7–9]

Two-dimensional (2D) nanostructures, an emerging family of new nanomaterials, have piqued the interest of researchers because of their unique morphological and physicochemical characteristics.[10–15] For example, graphene, the first 2D nanomaterial and its derivatives have been found to possess a broad solar absorption band with a high photothermal conversion efficiency (PTCE) ranging from 80% to 83%,[16–18] while its ultrathin thickness (less than 2 nm) can be used to fabricate large-area solar absorbers with only a small quantity of starting materials required. Recently, Ren *et al.*[19] have demonstrated that by integrating copper nanoparticles into graphene materials the PTCE for solar evaporation can be enhanced when compared to pristine material. However, the synthesis of graphene-based nanomaterials generally required expensive starting materials and complicated synthesis steps, and it was difficult to scale them up for realistic use in solar absorbers.[20,21]

Dr Edison Huixiang Ang obtained his PhD from Nanyang Technological University (NTU, Singapore). He worked as a Postdoctoral Fellow at both the National University of Singapore and NTU, and was also a Visiting Scholar at the Technical University of Munich, Germany. He is currently an assistant professor at NTU, and his research interests combine nanotechnology and materials science approaches to develop functional nanostructures for energy storage and conversion, as well as water treatment applications. He was honoured with the prestigious IAAM Young Scientist Medal Award (2022), the Vebleo Fellow Award (2021) and the Outstanding ASIAN Science Diplomat Award (2021).

[a]Natural Sciences and Science Education, National Institute of Education, Nanyang Technological University, Singapore 637616, Singapore. E-mail: edison.ang@nie.edu.sg

[b]School of Materials Science and Engineering, Nanyang Technological University, Singapore 639798, Singapore. E-mail: MIYTok@ntu.edu.sg

[c]School of Chemical and Biomedical Engineering, Nanyang Technological University, Singapore 637459, Singapore

[d]Department of Chemistry, Indian Institute of Science Education and Research Thiruvananthapuram, Kerala 695551, India

[e]School of Materials Engineering, Changshu Institute of Technology, Changshu, Jiangsu, 215500, PR China

[f]Faculty of Chemistry, Northeast Normal University, Changchun, Jilin, 130024, PR China

† Electronic supplementary information (ESI) available: Detailed methods and further characterizations include. See https://doi.org/10.1039/d2ta02092k

‡ These authors contributed equally to the work.

Previous studies have shown that simple hydrothermal carbonization and solvothermal methods can convert polymeric materials into amorphous carbon nanoparticles,[22–24] but there has yet to be a demonstration of converting plastic wastes into ultrathin carbon nanosheets (CNS) with a graphitic-like structure using such simple processes. In this study, we present a simple two-step method for fabricating 2D graphitic carbon nanosheets (g-CNS) from plastic waste (see Fig. 1a), and the resulting 2D g-CNS has an ultrathin thickness that is sub-1 nm. Common household plastic wastes (see Fig. S1, ESI†) such as plastic bags (PB), laundry detergent bottles (LB) and Tupperware containers (TC) made up of different plastic recycling grades such as low-density poly(ethylene) (LDPE), high-density poly(ethylene) (HDPE) and poly(propylene) (PP), respectively, are used as starting materials to make 2D g-CNS. These plastic wastes were selected for this study because they have a long decomposition period ranging from 20 to 100 years, are resistant to degradation, and are not easily recyclable, all of which have a negative environmental impact.[25] The preliminary results show that different 2D g-CNS derived from various types of plastic waste have different PTCE, and the one that is derived from PB exhibits the highest PTCE. The as-fabricated 2D g-CNS solar absorber derived from PB presents an efficient PTCE of 99% with a high evaporation rate of 1.50 kg m^{-2} h^{-1} under one-sun illumination, because of its broad solar absorption band (300–1600 nm), excellent photothermal properties, high heat retention, good wetting ability, well-organized interlayer channels, and availability of a wide range of micro- and mesopores for fast water transportation. This is the first time, such superior PTCE and evaporation rates have been obtained, when compared to data in the literature (Table S1, ESI†). The typical preparation procedure of 2D g-CNS is illustrated in Fig. 1. To illustrate our synthesis procedure, PB waste is used as an example. In Stage I, the s-CB_{PB} was prepared using a solvothermal treatment on a mixture of PB waste and sulfuric acid precursors at 110 °C. In brief, the sulfuric acid oxidizes and dehydrogenates the polymer chains, forming a sulfonic acid functional group.[26,27] This can be shown by the presence of $-SO_3H$ functional groups in the attenuated total reflection-Fourier transform infrared (ATR-FTIR) spectra (Fig. S2a–c, ESI†). At an elevated temperature, saturated carbon polymer chains are formed and crosslinked *via* either physical (*i.e.*, van der Waals forces) or chemical (*i.e.*, covalent, π–π interaction) interactions,[28] forming a sulfonated graphitic-like precursor, namely, s-CB_{PB}. The X-ray diffraction (XRD) characterization (Fig. S3a–c, ESI†) further confirmed the formation of a graphitic structure in the s-CB samples. Subsequently, the as-obtained sulfonated precursors were carbonized at 900 °C under an H_2/Ar gas flow to remove any remaining $-H_2$, $-CO$, $-CO_2$, $-H_2O$ and SO_2 functional groups, yielding 2D g-CNS_{PB}. More importantly, it also demonstrated that this strategy can be employed to prepare 2D graphitic nanosheets from other plastic wastes, such as LB and TC (see the ESI in the ESI† for details).

For the first time, these graphitic 2D CNS were fabricated from plastic wastes. The unique graphitic-like and 2D structures do not appear in previously reported carbonaceous materials originated from plastic waste.[29,30] Because of the merits of the graphitic-like characteristics and the 2D interlayer channel architecture this can improve (i) the light-to-heat conversion, and (ii) the water transport for solar evaporation, respectively, as illustrated in Fig. 1b.

The XRD patterns (Fig. 2a) of 2D g-CNS_{PB} show two distinct diffraction peaks of 26.1° (002) and 45.0° (101) which can be indexed to hexagonal graphitic carbon (JCPDS no. 56-0159). This result indicates that we have successfully synthesized graphitic carbon after carbonization at 900 °C under an H_2/Ar atmosphere. In addition, the distinct diffraction peak at $2\theta = 31.2°$, corresponding to (020) plane that can be indexed to the cubic CaC_2 crystal structure (JCPDS no. 15-4081).

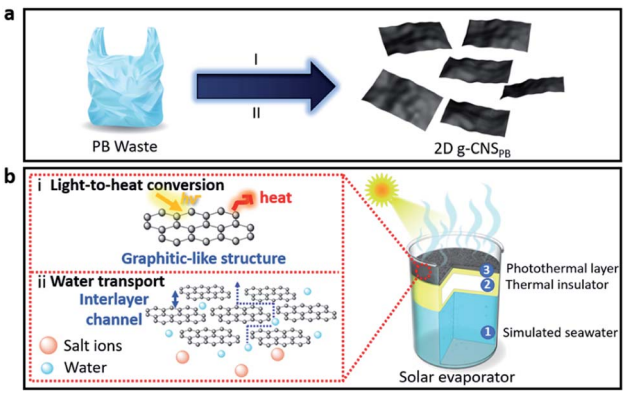

Fig. 1 (a) Schematic illustration of the formation of 2D graphitic carbon nanosheets (g-CNS) from upcycling of PB waste. Stage I: growth of sulfonated carbon black derived from plastic bag (s-CB_{PB}). Stage II: formation of 2D g-CNS_{PB} by carbonization of s-CB_{PB}. (b) The schematic shows a typical setup of a solar evaporator and the unique features of the 2D g-CNS_{PB} consisting of: (1) simulated seawater, (2) a thermal insulator (*i.e.*, polystyrene, PS foam), and (3) a photothermal layer made up of 2D g-CNS on an air-laid paper support.

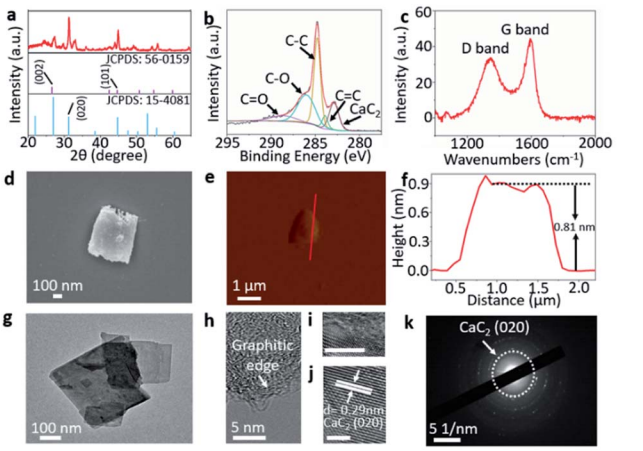

Fig. 2 (a) The XRD patterns of the 2D g-CNS_{PB} product, which agree well with the standard pattern of graphite and CaC_2. (b) High resolution C 1s XPS spectrum, (c) Raman spectrum, and (d) SEM image of g-CNS_{PB}. (e) AFM image of g-CNS_{PB} with its corresponding (f) height profile. (g) Low magnification TEM image, (h) high-magnification image, (i and j) HRTEM images with scale bars 5 nm and 2 nm, respectively, and (k) SAED pattern of a g-CNS_{PB} sample.

The chemical structures of 2D g-CNS_{PB} were further examined by X-ray photoelectron spectroscopy (XPS) analysis (Fig. 2b). The XPS C 1s spectrum shows the peaks at binding energies of 283, 284, 284.8, 286, and 289 eV, which correspond to CaC_2, C═C, C–C, C–O and C═O bonds, respectively. This series of carbon species matches the carboxylic and saturated carbon functional groups in the 2D g-CNS_{PB}. Moreover, the Raman spectrum of 2D g-CNS_{PB} (Fig. 2c) reveals two significant peaks at *ca.* 1350 cm^{-1} and *ca.* 1580 cm^{-1}, which are attributed to the D and G bands, respectively, of the graphene-based materials.[31] This result is in agreement with the XRD pattern, and further confirmed that graphitic carbon materials were obtained successfully. The field-emission scanning electron microscopy (FESEM) image, transmission electron microscopy (TEM) image and atomic force microscopy (AFM) image (Fig. 2d–g) with its height profile, prove that the obtained 2D g-CNS_{PB} possesses a lateral size (micrometer scale) with a thickness of 0.81 nm. The formation of such ultrathin nanosheets was achieved by a simple solvent exfoliation method,[32,33] as shown in Fig. S4, ESI†. The high-resolution (HR)-TEM image (Fig. 2h) shows that the 2D g-CNS_{PB} is composed of graphitic edges, and a hybrid of amorphous and crystalline regions can be observed in Fig. 2i, where the latter shows an interplanar spacing of 0.29 nm (see Fig. 2j), which corresponds to the (020) plane of CaC_2. The ring-like pattern observed in the selected area electron diffraction (SAED) indicates that the CaC_2 is polycrystalline in nature (Fig. 2k). After replacing PB with LB and TC wastes, the XRD patterns (Fig. S5a and b, ESI†), XPS spectra (Fig. S6a and b, ESI†) and Raman spectra (Fig. S7a and b, ESI†) show the same graphitic and carboxylic features as 2D g-CNS_{PB}. However, CaC_2 can only be detected in 2D g-CNS_{PB} and 2D g-CNS_{LB} samples but not in the 2D g-CNS_{Tc} sample. This is because in some of the plastic production line, CaC_2 is employed as a raw material to produce acetylene, which is used to make several plastic materials, for example, polyethylene.[34] In addition, the AFM, TEM and HRTEM images reveal that the sheet-like structure of g-CNS_{LB} and g-CNS_{TC} samples have a lateral dimension at the micrometer scale with ultrathin thicknesses of less than 1.0 nm (Fig. S8a–d, ESI†), and both samples exhibit graphitic edges (Fig. S9a–d, ESI†). Based on the Brunauer–Emmett–Teller (BET) model, the specific surface areas of 2D g-CNS_{PB}, 2D g-CNS_{LB} and 2D g-CNS_{TC} samples are 272.12, 254.64 and 6.24 $m^2\ g^{-1}$, respectively, and the nonlocal density functional theory (NLDFT) plots indicate the presence of micro-meso porosity in the samples with a pore width of less than 10 nm (Fig. S10a–f, ESI†). The photothermal layer comprises a solar absorber (*i.e.*, 2D g-CNS_{PB}) prepared on an air-laid paper support. The photograph (Fig. 3a) shows that the resultant 2D g-CNS_{PB} photothermal layer (*ca.* 3.5 cm in diameter) is evenly coated on the air-laid paper support with a mass loading of 0.10 kg m^{-2}. The energy dispersive X-ray spectroscopy (EDX) mapping images of the 2D g-CNS_{PB} photothermal layer show a uniform compositional distribution of C, O and Ca elements on the solar absorber. The absorption spectrum of the 2D g-CNS_{PB} solar absorber shows an excellent solar absorption of 86–99% at a wavelength of 300–1600 nm (Fig. 3c), and its thermal image (Fig. 3d) reveals a temperature of 53.1 °C under one-sun illumination. These results indicate that the 2D g-CNS_{PB} solar absorber possesses photothermal properties, which are essential for solar evaporation applications. For comparison, the uniform coatings of 2D g-CNS_{LB} and 2D g-CNS_{TC} solar absorbers on an air-laid paper support are shown in the photographs (see Fig. S11a and b, ESI†), and their surface morphologies and elemental distributions were also examined using FESEM and EDX analyses (Fig. S12a and b, ESI†). In addition, the solar absorptions of 2D g-CNS_{LB} and 2D g-CNS_{TC} photothermal layers were in the ranges of 54–60% and 41–56%, respectively, (Fig. S13a and b, ESI†). The temperatures of 2D g-CNS_{LB} and 2D g-CNS_{TC} photothermal layers were 43.5 °C and 41.7 °C, respectively, (Fig. S14a and b, ESI†), while the control experiment consisting of air-laid paper without a solar absorber shows a stable temperature at room temperature under one-sun illumination (Fig. S15, ESI†). These results further confirmed that the as-obtained solar absorbers possess photothermal properties. A home-made solar evaporator (Fig. S16, ESI†) was used to measure the water evaporation rates, enhancement factor and PTCE of 2D g-CNS_{PB}, 2D g-CNS_{LB} and 2D g-CNS_{TC} photothermal layers under one-sun illumination.

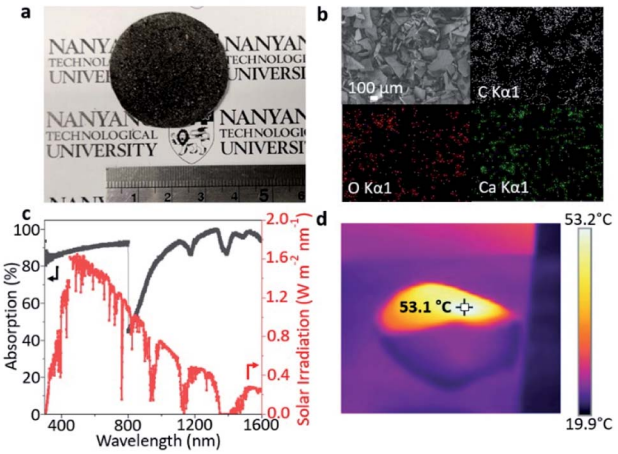

Fig. 3 (a) Photograph of 2D g-CNS_{PB} deposited on air-laid paper, (b) FESEM image of a 2D g-CNS_{PB} photothermal layer with its corresponding EDX mapping images of C, O and Ca elements, (c) UV-vis-NIR absorption spectrum of 2D g-CNS_{PB} with AM 1.5 solar irradiance as a reference. (d) Thermal image of the 2D g-CNS_{PB} photothermal layer under air.

To investigate the performances of the solar evaporators consisting of g-CNS solar absorbers, air-laid paper/PS foam on simulated seawater (3.5 wt%), water evaporation rate (m, kg $m^{-2}\ h^{-1}$), enhancement factor (EF) and PTCE (%) are tabulated using eqn (1), (2) and (3), respectively. As a reference experiment, a control solar evaporator is utilized consisting of the air-laid paper/PS foam on simulated seawater without the g-CNS solar absorber.

$$m = \frac{\Delta m}{S \times t} \quad (1)$$

where Δm refers to the mass change of water (kg), S refers to the area of the photothermal layer (m^2), and t refers to the solar illumination time (h).

$$\mathrm{EF} = \frac{m(\mathrm{SE})}{m(\mathrm{blank})} \quad (2)$$

where m(SE) refers to either the water evaporation rate of g-CNS or the control solar evaporators, and m(blank) refers to the water evaporation rate of simulated seawater under one-sun illumination.

In addition, the PTCE (%) performance of the solar evaporators is calculated using the following eqn (3):

$$\mathrm{PTCE} = \frac{m' \times h_{\mathrm{LV}}}{P_{\mathrm{in}}} \quad (3)$$

where m' (kg m^{-2} h^{-1}) refers to m(SE) minus the water evaporation rate of simulated seawater in the dark, h_{LV} is the total enthalpy of vaporization (refer to details in Section S1, ESI†), P_{in} is the incident solar power at 1 kW m^{-2} (= one-sun illumination).

The mass change of the simulated seawater was measured using an analytical balance and one-sun illumination was applied unless otherwise stated. As is known, the mass loading of the solar absorber can influence the solar evaporation rate, therefore, mass optimization was first carried out to obtain the optimum performances for all the 2D g-CNS samples (see Fig. S17, ESI†). In general, the water evaporation rates of the 2D g-CNS samples increased with the increase of mass loading, but a further increase in mass loading led to a reduction in the heat exchange velocity,[35,36] resulting in a slight decrease in water evaporation rate. For the subsequent performance measurements, the optimal mass loading for all the samples was used. The tests for mass loss due to water evaporation as a function of irradiation time were all performed for 60 min (see Fig. 4a). The cumulative mass loss was found to increase linearly with irradiation time. Under one-sun illumination, the 2D g-CNS$_{PB}$ solar evaporator presented a water evaporation rate of 1.50 kg m^{-2} h^{-1} which was 2.05, 1.06 and 1.15 times higher than that of the solar evaporators consisting of a control (0.73 kg m^{-2} h^{-1}), 2D g-CNS$_{LB}$ (1.41 kg m^{-2} h^{-1}) and 2D g-CNS$_{TC}$ (1.30 kg m^{-2} h^{-1}), respectively (Fig. 4b). The evaporation rate value obtained under dark conditions was 0.073 kg m^{-2} h^{-1} and this dark evaporation rate was subtracted from all the measured evaporation rates under solar illumination to isolate the effect of solar irradiation on the evaporation rate. In addition, the 2D g-CNS$_{PB}$, g-CNS$_{LB}$ and g-CNS$_{TC}$ solar evaporators *versus* the control exhibited EF values of 2.39, 2.25, 2.07 and 1.28, respectively (see Fig. 4c), and the PTCE percentages were 99%, 94%, 86% and 48%, respectively, (see Fig. 4d). These results show that the performances of 2D g-CNS solar evaporators in terms of water evaporation rates, EF and PTCE were improved almost 2-fold when compared to the control, which indicated the efficient photothermal properties of the as-prepared 2D g-CNS solar absorbers. To examine the durability of the 2D g-CNS solar evaporator, the steady-state cumulative mass loss was found to be negligible after 15 cycles of reuse, which indicated the robust stability of the as-fabricated solar absorber (Fig. S18, ESI†). Compared with the state-of-the-art solar evaporators (including carbonaceous, inorganic/ceramic, commercial solar absorbers), our 2D g-CNS solar evaporators, especially 2D g-CNS$_{PB}$, exhibited superior water evaporation rates and PTCE performances (see Fig. 5 and Table S1, ESI†). Several solar evaporators exhibited either a high water evaporation rate or a high PTCE. Among them all, the present 2D g-CNS$_{PB}$ solar evaporator not only showed a high water evaporation rate of 1.50 kg m^{-2} h^{-1}, but also delivered an exceptionally high PTCE of 99%. In addition, it also gave rise to excellent water evaporation rate and PTCE, which were almost 60% and 50% higher than those of the commercial solar evaporator consisting of a carbonized membrane (CM). To investigate the excellent PTCE of the 2D g-CNS solar evaporators, further heat loss experiments were also conducted (see details in Section S2, ESI†). The heat loss results showed that

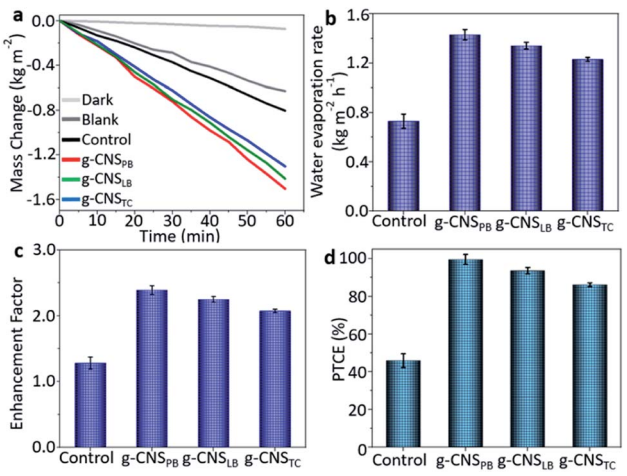

Fig. 4 (a) Cumulative mass change of simulated seawater *versus* time under various conditions: water in dark (dark), water under solar irradiation (blank), water with air-laid paper/PS foam (control), different g-CNS solar evaporators under one-sun solar illumination. (b) Water evaporation rates. (c) Enhancement factors, and (d) PTCE diagrams of the control and different g-CNS solar evaporators.

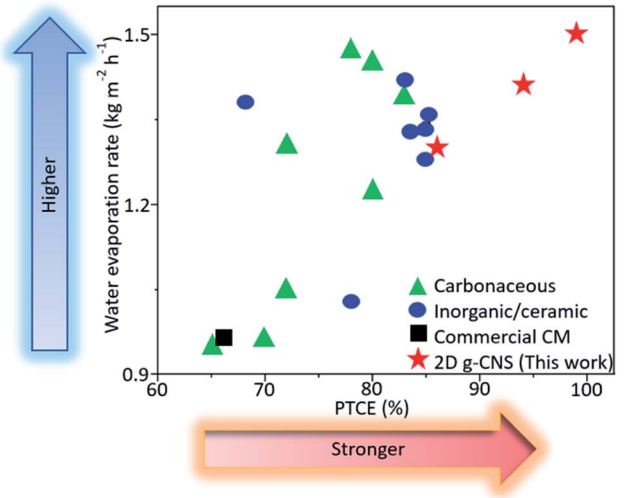

Fig. 5 Comparison of solar vapor generation performances of 2D g-CNS solar evaporators with previously reported solar evaporators under one-sun illumination (see details in Table S1, ESI†).

the 2D g-CNS_{PB} solar evaporator had a low heat loss of 14.1%, which was the sum of heat radiation (6.3%), heat convection (5.0%) and heat conduction (2.8%). This value was close to the heat losses of 2D g-CNS_{LB} (13.5%) and 2D g-CNS_{TC} (9.9%) solar evaporators, and indicated that there was suitable thermal management.

To understand the mechanisms resulting in the excellent water evaporation rates, the contact angles of 2D g-CNS (*i.e.*, g-CNS_{PB}, g-CNS_{LB} and g-CNS_{TC}) solar evaporators were characterized and the results are summarized in (Fig. S19a–c, ESI†). Among the 2D g-CNS photothermal layers, the g-CNS_{PB} photothermal layer has a smaller contact angle when compared to the other two g-CNS photothermal layers (*i.e.*, g-CNS_{LB} and g-CNS_{TC}). The XPS measurements (Table S2, ESI†) showed that the 2D g-CNS_{PB} sample contained a higher oxygenated functional group content (*i.e.*, C=O and C–O) when compared to g-CNS_{LB} and g-CNS_{TC} samples, and it was reasonable that a higher density of oxygenated functional groups on the 2D g-CNS was responsible for the high hydrophilicity ability.[37] The good wetting properties of the photothermal layer provided numerous hydrophilic sites for water to access, thus, increasing the rate of water evaporation.[38,39] In addition, the XRD measurements were employed to elucidate the degree of organization of channels of the 2D g-CNS samples (compare Fig. 2a and S5a, b, ESI†). As such, the g-CNS_{PB} sample showed a narrower graphitic peak when compared to those of the rest of the g-CNS samples, which suggested the former had a well-organized interlayer channel. This was further verified by the high intensity ratio of the G and D bands (I_G/I_D) derived from the Raman measurements (Table S3, ESI†). The presence of a side branch in the LDPE polymer (Table S1, ESI†) allowed the neighboring polymers to crosslink during the solvothermal treatment and carbonization processes,[40] resulting in a higher structural ordering in g-CNS_{PB} than in the other two g-CNS samples. As is known, the highly ordered interlayer channel facilitated fast water transport, but the disordered ones increased the flow resistance of the water transport.[41] This further explained the scientific reasoning for the outstanding water evaporation rate of the g-CNS_{PB} solar evaporator, as shown in Fig. 5. In addition, the NLDFT pore size distribution measurement of the 2D g-CNS_{PB} sample showed a higher pore volume of micro- and mesopores when compared to the other 2D g-CNS samples (Fig. S10d–f, ESI†). This observation implied that there were numerous channels for water to enter, resulting in the higher water evaporation rate of the 2D g-CNS_{PB} solar evaporator when compared to 2D g-CNS_{LB} and 2D g-CNS_{TC} solar evaporators.

To understand the PTCE performances of the 2D g-CNS solar evaporators shown in Fig. 5, thermal analyses were also performed on the g-CNS solar evaporators under one-sun illumination (Fig. S20a–c, ESI†). The results showed that the g-CNS_{PB} solar evaporator exhibited a high photothermal temperature of 35 °C on the water surface, which was higher than that of the g-CNS_{LB} and g-CNS_{TC} solar evaporators. For comparison purposes, the control showed a photothermal temperature of approximately 25 °C (Fig. S21, ESI†) in the presence of solar illumination. These observations further confirmed the photothermal characteristics of the as-prepared 2D g-CNS samples. The superior PTCE performances of the g-CNS_{PB} solar evaporator over the other g-CNS solar evaporators could also be attributed to the broad solar absorption bandwidth and high absorption percentage of the g-CNS_{PB} materials (see Fig. 3c), which implied that the g-CNS_{PB} sample has significant optical properties in the solar wavelength range. The broad light absorption of the g-CNS materials can be attributed to their high pore volume, which trapped multiple light scattering within the porous structure, resulting in highly localized heating. It is worth noting that when using the same mass loading (0.08 kg m^{-2}) of the g-CNS solar absorber, the hydrophilicity and light absorption properties of all three g-CNS samples follow a similar trend as the optimum mass loading (compare Fig. S13,S19, S22, and S23, ESI†). As is known, water evaporation occurs at the interface between water molecules and air. Compared to other reported thermal conductivity values (0.113–0.119 W m^{-1} K^{-1}),[42–44] the 2D g-CNS photothermal layers exhibited a lower thermal conductivity ranging from 0.044–0.059 W m^{-1} K^{-1}, which indicating a better heat retention, resulting in the superb solar vapour generation, as shown in Fig. 5. Furthermore, as the solar illumination time was increased, the surface temperature of 2D g-CNS_{PB} rapidly increased to about 53.1 °C and then remained constant, demonstrating the excellent heat retention of the as-prepared g-CNS samples (Fig. S24, ESI†).

Conclusions

In summary, we have developed a novel strategy to convert household plastic bag waste into 2D ultrathin carbon nanosheets with a thickness of less than *ca.* 1 nm. This method has also been successfully extended to other plastic wastes such as laundry detergent bottles and Tupperware containers. Benefiting from the graphitic-like structure and organized interlayer channel, the 2D g-CNS_{PB} exhibits an excellent water evaporation rate of 1.50 L m^{-2} h^{-1} under one-sun illumination with a PTCE of 99%, which demonstrates the best water evaporation rate and PTCE when compared to the other state-of-the-art materials. Moreover, the 2D g-CNS_{PB} solar evaporator shows outstanding cycle stability after reuse for 15 times. The successful conversion of plastic waste into 2D graphitic nanosheets may pave the way for the development of more efficient solar evaporators. Such a distinct graphitic structure can be used in a variety of applications, including catalytic activities and energy conversion processes.

Author contributions

MA and RG contributed equally to this work. EHA conceived the idea and directed the project. All the authors commented on the manuscript and contributed to the discussion of the results.

Conflicts of interest

There are no conflicts to declare.

Acknowledgements

This work was supported by the National Institute of Education, Singapore, under its Academic Research Fund (RI 1/21 EAH), and the National Institute of Education, Singapore, under its Start-Up Grant (NIE-SUG4/20AHX).

Notes and references

1 R. Geyer, J. R. Jambeck and K. L. Law, *Sci. Adv.*, 2017, **3**, e1700782.
2 M. MacLeod, H. P. H. Arp, M. B. Tekman and A. Jahnke, *Science*, 2021, **373**, 61–65.
3 A. Gómez-Sanabria, G. Kiesewetter, Z. Klimont, W. Schoepp and H. Haberl, *Nat. Commun.*, 2022, **13**, 106.
4 Z. Wen, Y. Xie, M. Chen and C. D. Dinga, *Nat. Commun.*, 2021, **12**, 425.
5 I. Vollmer, M. J. F. Jenks, M. C. P. Roelands, R. J. White, T. van Harmelen, P. de Wild, G. P. van der Laan, F. Meirer, J. T. F. Keurentjes and B. M. Weckhuysen, *Angew. Chem., Int. Ed.*, 2020, **59**, 15402–15423.
6 N. Vora, P. R. Christensen, J. Demarteau, N. R. Baral, J. D. Keasling, B. A. Helms and C. D. Scown, *Sci. Adv.*, 2021, **7**, eabf0187.
7 K. L. Law and R. Narayan, *Nat. Rev. Mater.*, 2022, **7**, 104–116.
8 E. Barnard, J. J. Rubio Arias and W. Thielemans, *Green Chem.*, 2021, **23**, 3765–3789.
9 J. J. Rubio Arias and W. Thielemans, *Green Chem.*, 2021, **23**, 9945–9956.
10 Z. Xie, Y. Duo, Z. Lin, T. Fan, C. Xing, L. Yu, R. Wang, M. Qiu, Y. Zhang and Y. Zhao, *Adv. Sci.*, 2020, **7**, 1902236.
11 S. Jiang, L. Li, Z. Wang, K. F. Mak and J. Shan, *Nat. Nanotechnol.*, 2018, **13**, 549–553.
12 D. Xu, D. Chao, H. Wang, Y. Gong, R. Wang, B. He, X. Hu and H. J. Fan, *Adv. Energy Mater.*, 2018, **8**, 1702769.
13 H. Zhang, M. Chhowalla and Z. Liu, *Chem. Soc. Rev.*, 2018, **47**, 3015–3017.
14 C. Rao, H. Ramakrishna Matte and U. Maitra, *Angew. Chem., Int. Ed.*, 2013, **52**, 13162–13185.
15 Z. Wang, Q. Lin, F. P. Chmiel, N. Sakai, L. M. Herz and H. J. Snaith, *Nat. Energy*, 2017, **2**, 17135.
16 H. Ren, M. Tang, B. Guan, K. Wang, J. Yang, F. Wang, M. Wang, J. Shan, Z. Chen, D. Wei, H. Peng and Z. Liu, *Adv. Mater.*, 2017, **29**, 1702590.
17 X. Zhou, F. Zhao, Y. Guo, Y. Zhang and G. Yu, *Energy Environ. Sci.*, 2018, **11**, 1985–1992.
18 H. Lin, B. C. P. Sturmberg, K.-T. Lin, Y. Yang, X. Zheng, T. K. Chong, C. M. de Sterke and B. Jia, *Nat. Photonics*, 2019, **13**, 270–276.
19 L. Ren, X. Yi, Z. Yang, D. Wang, L. Liu and J. Ye, *Nano Lett.*, 2021, **21**, 1709–1715.
20 A. N. Obraztsov, *Nat. Nanotechnol.*, 2009, **4**, 212–213.
21 W. Yu, L. Sisi, Y. Haiyan and L. Jie, *RSC Adv.*, 2020, **10**, 15328–15345.
22 N. Huang, P. Zhao, S. Ghosh and A. Fedyukhin, *Appl. Energy*, 2019, **240**, 882–892.
23 D. Ma, Q. Feng, B. Chen, X. Cheng, K. Chen and J. Li, *J. Hazard. Mater.*, 2019, **380**, 120847.
24 C. Yuwen, B. Liu, Q. Rong, L. Zhang and S. Guo, *Sci. Total Environ.*, 2022, **817**, 152995.
25 M. Ilyas, W. Ahmad, H. Khan, S. Yousaf, K. Khan and S. Nazir, *Rev. Environ. Health*, 2018, **33**, 383–406.
26 M. A. Hunt, T. Saito, R. H. Brown, A. S. Kumbhar and A. K. Naskar, *Adv. Mater.*, 2012, **24**, 2386–2389.
27 M. Kaneko, S. Kumagai, T. Nakamura and H. Sato, *J. Appl. Polym. Sci.*, 2004, **91**, 2435–2442.
28 B. E. Barton, J. Patton, E. Hukkanen, M. Behr, J.-C. Lin, S. Beyer, Y. Zhang, L. Brehm, B. Haskins and B. Bell, *Carbon*, 2015, **94**, 465–471.
29 F. Liu, L. Wang, R. Bradley, B. Zhao and W. Wu, *RSC Adv.*, 2019, **9**, 29414–29423.
30 X. Liu, S. He, Z. Han and C. Wu, *Process Saf. Environ. Prot.*, 2021, **146**, 201–207.
31 J. Gong, H. Lin, M. Antonietti and J. Yuan, *J. Mater. Chem. A*, 2016, **4**, 7313–7321.
32 J. N. Coleman, M. Lotya, A. O'Neill, S. D. Bergin, P. J. King, U. Khan, K. Young, A. Gaucher, S. De, R. J. Smith, I. V. Shvets, S. K. Arora, G. Stanton, H.-Y. Kim, K. Lee, G. T. Kim, G. S. Duesberg, T. Hallam, J. J. Boland, J. J. Wang, J. F. Donegan, J. C. Grunlan, G. Moriarty, A. Shmeliov, R. J. Nicholls, J. M. Perkins, E. M. Grieveson, K. Theuwissen, D. W. McComb, P. D. Nellist and V. Nicolosi, *Science*, 2011, **331**, 568–571.
33 V. Nicolosi, M. Chhowalla, M. G. Kanatzidis, M. S. Strano and J. N. Coleman, *Science*, 2013, **340**, 1226419.
34 S. P. Teong and Y. Zhang, *J. Bioresour. Bioprod.*, 2020, **5**, 96–100.
35 Y. Zeng, J. Yao, B. A. Horri, K. Wang, Y. Wu, D. Li and H. Wang, *Energy Environ. Sci.*, 2011, **4**, 4074–4078.
36 J. Wang, Z. Liu, X. Dong, C.-E. Hsiung, Y. Zhu, L. Liu and Y. Han, *J. Mater. Chem. A*, 2017, **5**, 6860–6865.
37 J. Yang, Y. Pang, W. Huang, S. K. Shaw, J. Schiffbauer, M. A. Pillers, X. Mu, S. Luo, T. Zhang, Y. Huang, G. Li, S. Ptasinska, M. Lieberman and T. Luo, *ACS Nano*, 2017, **11**, 5510–5518.
38 E. H. Ang, S. Velioğlu and J. W. Chew, *J. Membr. Sci.*, 2019, **591**, 117318.
39 H. Ang and L. Hong, *ACS Appl. Mater. Interfaces*, 2017, **9**, 28079–28088.
40 J. H. Eun and J. S. Lee, *Sci. Rep.*, 2021, **11**, 18028.
41 K. Falk, F. Sedlmeier, L. Joly, R. R. Netz and L. Bocquet, *Nano Lett.*, 2010, **10**, 4067–4073.
42 C. Song, L. Hao, B. Zhang, Z. Dong, Q. Tang, J. Min, Q. Zhao, R. Niu, J. Gong and T. Tang, *Sci. China Mater.*, 2020, **63**, 779–793.
43 B. Zhang, C. Song, C. Liu, J. Min, J. Azadmanjiri, Y. Ni, R. Niu, J. Gong, Q. Zhao and T. Tang, *J. Mater. Chem. A*, 2019, **7**, 22912–22923.
44 C. Song, B. Zhang, L. Hao, J. Min, N. Liu, R. Niu, J. Gong and T. Tang, *Green Energy Environ.*, 2022, **7**, 411–422.